

---

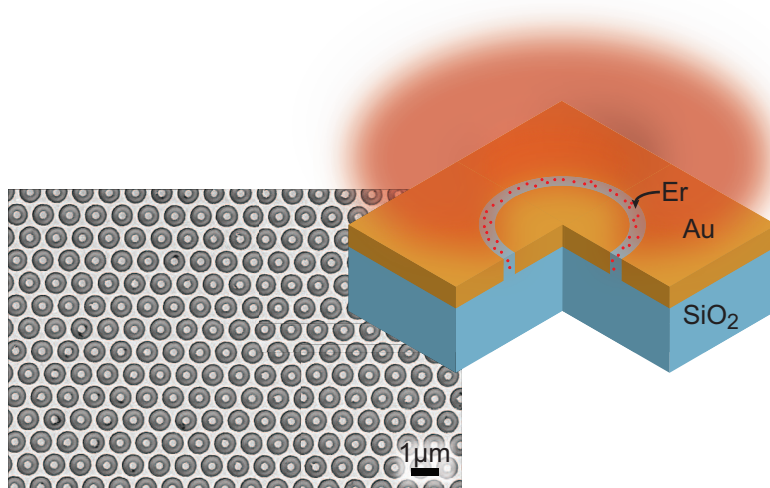
# Enhanced spontaneous emission rate in annular plasmonic nanocavities

E. J. A. Kroekenstoel

*Supervisors:*

Drs. E. Verhagen and Prof. Dr. A. Polman

---



Research project for the masters degree in  
*Nanomaterials: Chemistry and Physics*  
at Utrecht University, The Netherlands  
September 2008 - August 2009

Center for Nanophotonics  
FOM Institute AMOLF  
Amsterdam, The Netherlands



FOM Institute  
**AMOLF**



## Abstract

Control of spontaneous emission is of interest for many applications, including LEDs, sensors, quantum information processing and photovoltaics. By modifying the local electromagnetic environment of an optical emitter, the polarization and the directionality of its radiation as well as its overall decay rate can be modified.

In this work, we study spontaneous emission from Er in subwavelength annular apertures in a Au film. These annular apertures support a localized plasmonic resonance. It is shown that this resonance is due to cutoff of the  $TE_{11}$  mode in an annular waveguide and that its wavelength can be tuned by varying the average radius of the annular aperture. We employ finite difference time domain simulations to confirm the existence and tunability of the resonance as well as to determine the optimal size and shape of the apertures.

The localized resonance causes the annular apertures to act as nanocavities with modal field confined to the apertures. Electron beam lithography and reactive ion etching are employed to selectively position Er ions, embedded in  $SiO_2$ , inside apertures in a Au film. The nanocavities enhance the local density of states at the Er emission wavelength of  $1.54\ \mu m$  when they are tuned to that wavelength. We show that this leads to an 8-fold increase of the photoluminescence intensity, in conjunction with a 2.4-fold enhancement of the spontaneous emission decay rate.



# Contents

<b>1</b>	<b>Introduction</b>	<b>1</b>
1.1	Controlling spontaneous emission . . . . .	1
1.2	Thesis outline . . . . .	1
<b>2</b>	<b>Enhanced spontaneous emission rate in annular plasmonic nanocavities</b>	<b>3</b>
<b>3</b>	<b>Localized resonance in annular apertures</b>	<b>9</b>
3.1	Introduction . . . . .	9
3.2	Controlling spontaneous emission . . . . .	9
3.3	Finite difference time domain simulations . . . . .	10
3.3.1	Experimental . . . . .	11
3.3.2	Results . . . . .	11
3.4	Rayleigh-Wood anomalies . . . . .	16
3.5	Conclusion . . . . .	16
<b>4</b>	<b>Fabrication of Er-filled annular apertures in a metal film</b>	<b>17</b>
4.1	Introduction . . . . .	17
4.2	Fabrication steps . . . . .	17
4.3	Lift-off . . . . .	19
4.4	Conclusion . . . . .	20
<b>5</b>	<b>Spontaneous emission of Er in nanocavities</b>	<b>21</b>
5.1	Introduction . . . . .	21
5.2	Experimental . . . . .	21
5.2.1	Transmission . . . . .	21
5.2.2	Photoluminescence . . . . .	22
5.3	Results . . . . .	24
5.3.1	Transmission . . . . .	24
5.3.2	Photoluminescence . . . . .	24
5.4	Discussion . . . . .	25
5.5	Conclusion . . . . .	26
	<b>Bibliography</b>	<b>26</b>
	<b>Acknowledgements</b>	<b>29</b>

# Chapter 1

## Introduction

Spontaneous emission is the process of an excited atom, or other light source, emitting a photon and thereby falling back to its ground state. It plays an essential role in many phenomena, including lighting, telecommunications, sensors and quantum information processing. As a result, control of the spontaneous emission is of interest for many fields and applications.

### 1.1 Controlling spontaneous emission

By modifying the local electromagnetic environment of an emitter the polarization and the directionality of its radiation as well as its overall decay rate can be modified. The decay rate is related to the local density of optical states (LDOS) via Fermi's golden rule

$$\Gamma = \frac{2\pi}{\hbar} |\langle f | H | i \rangle|^2 \rho(\vec{x}, \omega) \quad (1.1)$$

where  $\rho$  is the local density of optical states and  $\langle f | H | i \rangle$  is a coupling term. [1] This local density of states describes the number of states per unit volume that the atom can decay into. The coupling term is mostly determined by the local chemistry and can not be arbitrarily influenced. The LDOS term on the other hand is a characteristic for a photonic structure and is very much dependent on the structure's shape. It is the local density of optical states that allows us to modify the spontaneous emission rate.

One of the possibilities for controlling the local density of states is making use of surface plasmon polaritons (SPPs). These are collective oscillations of free electrons at the boundary of a metal and a dielectric. [2] As such they can be regarded as electromagnetic waves at a metal-dielectric interface and their strong localization allows for subwavelength control of light. [3]

In this work we will consider the spontaneous emission of erbium in annular apertures in a metal film. Erbium is well known for its intra-4f transition in  $\text{Er}^{3+}$  ions that corresponds to a wavelength of  $1.54 \mu\text{m}$ , [4] because of the low losses of silica optical fibers at that wavelength.

### 1.2 Thesis outline

Chapter 2 is a manuscript to be submitted to Applied Physics Letters presenting the main results of this work. It contains a brief discussion of the localized resonance in annular apertures, the experimental methods, results and a discussion of the results. We demonstrate an

8-fold increase of the photoluminescence intensity, in conjunction with a 2.4-fold enhancement of the spontaneous emission decay rate. In the third chapter we will consider the localized plasmonic resonance theoretically. An approximation of the resonance wavelength in a perfect electric conductor is derived. Furthermore, we demonstrate the resonance's existence and tunability using finite difference time domain simulations. The fourth chapter discusses the fabrication of Er-filled annular apertures in a metal film. Chapter 5 will treat the experimental set-ups in more detail as well as present additional results not shown in Chapter 2.

## Chapter 2

# Enhanced spontaneous emission rate in annular plasmonic nanocavities

### Abstract

The spontaneous emission rate of erbium ions is enhanced by coupling to localized plasmonic resonances in subwavelength annular apertures fabricated in a Au film. The  $\text{Er}^{3+}$  ions, embedded in  $\text{SiO}_2$ , are selectively located inside the apertures. The annular apertures act as nanocavities enhancing the local density of optical states at the Er emission wavelength of  $1.54\ \mu\text{m}$  when the cavities are tuned to that wavelength. We show that this leads to an 8-fold increase of the photoluminescence intensity, in conjunction with a 2.4-fold enhancement of the spontaneous emission rate.

Control of spontaneous emission is of interest for many applications, including LEDs, sensors, quantum information processing and photovoltaics. By modifying the local electromagnetic environment of an optical emitter, the polarization and the directionality of its radiation as well as its overall decay rate can be modified. In recent years a number of different plasmonic geometries have been used to modify the spontaneous emission rate, including nanoparticles and nano-antennas. [5–12]

Suitably shaped subwavelength apertures in a metal film can also support a localized plasmonic resonance. For example, annular apertures, composed of an inner metal core, separated from the surrounding metal by a dielectric ring, can act as nanocavities with a modal field that is strongly confined to the aperture. [13–15] Even though the quality factor  $Q$  of these cavities is modest, the ultra small mode volume  $V$  can potentially lead to a significant Purcell enhancement of the spontaneous emission rate, which is given by [16]

$$F = \frac{3\lambda_0^3 Q}{4\pi^2 V}. \quad (2.1)$$

Because of the relatively low  $Q$ , the Purcell enhancement is observed over a large bandwidth. It is well known that annular apertures couple strongly to far-field radiation, since they can assist transmission of light through a metal film. [13–15] This makes these structures promising candidates for enhancing the radiative emission rate. Previous studies of fluorescence from subwavelength apertures have demonstrated the modification of spontaneous emission in various ways, [17–20] but these did not exploit localized resonances in the apertures.

In this work, we demonstrate the enhancement of the radiative emission rate of optically active erbium ions [4] positioned inside annular apertures in a gold film. We observe an increase in both PL intensity and decay rate as we tune the aperture's resonance wavelength to the Er transition wavelength. For the apertures with a resonance closest to the Er transition wavelength the total decay rate is increased by a factor 2.4, with respect to Er in a reference area: part of the sample without patterning or Au.

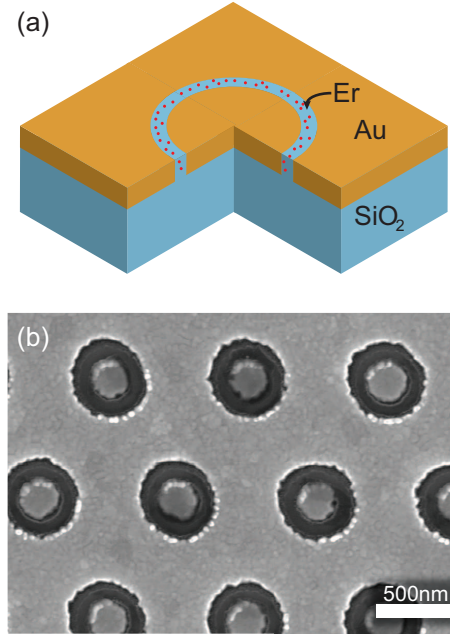


**Figure 2.1:** (a) Schematic of a single Er-doped SiO<sub>2</sub> annular aperture in a Au film on SiO<sub>2</sub>. (b) SEM image of a fabricated hexagonal array of annular apertures.

To obtain maximum spatial overlap of the Er ions with the nanocavity modal field the ions have to be positioned inside the annular apertures. A schematic of the fabricated structures is shown in Fig. 2.1(a). A fused silica (Heraeus Suprasil 300) substrate is first doped with erbium by 150 keV Er<sup>+</sup> ion implantation at normal incidence using a fluence of  $3.0 \times 10^{14} \text{ cm}^{-2}$ . This results in a distribution of Er ions at a mean depth of 82 nm with a standard deviation of 18 nm, as calculated with the Monte Carlo program SRIM. [21] The peak Er concentration is 0.29 at. %. We then remove the top 30 nm of silica with reactive ion etching in order to reduce the mean depth of the Er ions to 50 nm. Next, the substrate is covered with a resist stack of 500 nm PMMA, 20 nm Ge and 90 nm negative electron beam resist (Ma-N 2401) in which we pattern hexagonal arrays of annular structures by electron beam lithography. Square regions near these arrays are also exposed to provide reference areas. After developing the patterned layer, reactive ion etching through the resist layers and through 100 nm of silica is used to leave 100 nm thick Er-doped silica rings on the substrate. A 100 nm thick layer of gold is evaporated on the sample and the excess gold and resist is removed using lift-off. This results in annular apertures in a Au film on SiO<sub>2</sub>, filled with Er-doped SiO<sub>2</sub>. The apertures are arranged in  $50 \times 50 \mu\text{m}^2$  hexagonally ordered arrays. A top-view SEM image of part of such an array is depicted in Fig. 2.1(b). A small air gap is observed between the SiO<sub>2</sub> rings and Au surrounding.

Optical transmission spectra of the arrays are obtained by illuminating the sample from the air side with an NA of 0.02 and collecting the transmitted light through a 0.75 NA objective. The light is passed through a spectrometer and detected with either a silicon CCD for visible wavelengths or an InGaAs diode array for infrared light. Reflection spectra are recorded using a 0.65 NA reflective objective and a Biorad FTS6000 Fourier transform spectrometer with an InAs photodiode.

To measure the photoluminescence (PL) of the erbium ions the sample is illuminated with light from an argon ion laser operating at 488 nm incident under a 20° angle to the sample surface from the air side of the metal film. The light is focused to an elliptically shaped Gaussian spot with a full width at half maximum of 34  $\mu\text{m}$  along one direction and 85  $\mu\text{m}$  along the other, as measured using

a razor blade. The peak power density is  $275 \text{ W/cm}^2$  for intensity measurements and  $680 \text{ W/cm}^2$  for time-resolved measurements. We collect the luminescence with a 0.45 NA objective at the air side of the sample. PL intensity is measured with a spectrometer with an InGaAs diode array detector while measurements of the decay rate are performed with a North Coast EO-817s Ge photodiode detector with a response time of  $30 \mu\text{s}$ . The laser is modulated at 7 Hz with an acousto-optic modulator for decay rate measurements.

The resonance wavelength of the annular aperture nanocavities can be tuned by varying the aperture size and shape. The localized resonance that is considered here can be related to the  $\text{TE}_{11}$  mode of a coaxial waveguide with an equivalent cross section. [14, 15] At cutoff the wavevector of this mode becomes close to zero, resulting in resonant constructive interference inside the aperture for arbitrary film thickness. The cutoff wavelength for the  $\text{TE}_{11}$  mode in an annular waveguide in a perfect electric conductor is approximated by  $\lambda = n(R_o + R_i)\pi$ , [14, 15] where  $R_o$ ,  $R_i$  and  $n$  are the outer and inner radius of the aperture and the refractive index of the medium in the apertures, respectively. Here, we control the resonance wavelength by varying the average radius  $R = (R_o + R_i)/2$  from 193 to 303 nm. The width,  $R_o - R_i$ , of the annular apertures is kept constant at 100 nm to maintain a constant average separation between Er ions and the metal surface, and therefore a constant rate of direct quenching to the metal of excited Er. [22] Concurrent with the increase in  $R$  the periodicity is increased from 903 to 1086 nm such that the average areal density of Er ions is the same in all arrays, which simplifies the comparison of PL intensities.

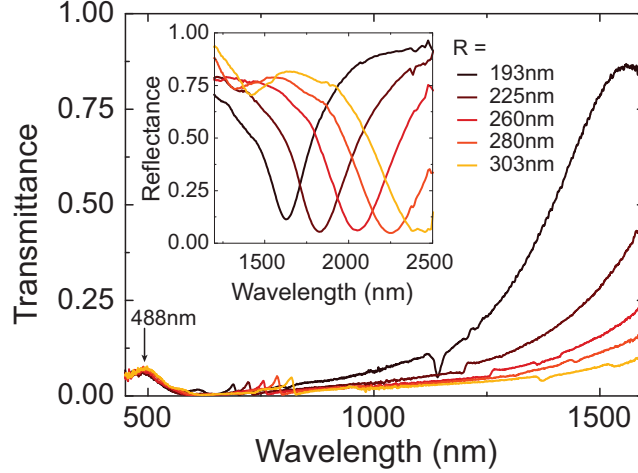


**Figure 2.2:** (a) Schematic of a single Er-doped  $\text{SiO}_2$  annular aperture in a Au film on  $\text{SiO}_2$ . (b) SEM image of a fabricated hexagonal array of annular apertures.

Transmission and reflection spectra of the arrays with varying  $R$  are shown in Fig. 2.2. A large transmittance peak is seen in conjunction with a dip in reflectance, associated with the localized resonance. As expected, the resonance wavelength shifts to larger wavelengths when  $R$  is increased. It varies from  $\sim 1.6 \mu\text{m}$  for the smallest radius to about  $2.4 \mu\text{m}$  for the largest radius. In Fig. 2.3(a) we plot the transmittance at  $1.54 \mu\text{m}$  for the different cavities as a function of the average radius  $R$ : it reduces from 0.84 to 0.08. As all transmission is mediated by the localized resonance, the transmittance can be used as a measure of the strength of the resonant mode at a given frequency. The decreasing transmittance for increasing  $R$  therefore implies that the local density of states at the Er transition wavelength will decrease as the radius is increased.

A typical PL spectrum of the  $\text{Er}^{3+} {}^4\text{I}_{13/2} \rightarrow {}^4\text{I}_{15/2}$  transition at  $1.54 \mu\text{m}$  is shown in Fig. 2.4(a). We compare the integrated PL intensity in Au annular nanocavities to that in similar arrays of silica rings that are not covered in Au. In Fig. 2.3(b) we plot the PL enhancement, taken as the ratio of the PL intensity from the Au nanocavities to that from the silica rings without Au for rings with different  $R$ . We observe an enhancement up to a factor 8 for the annular apertures with a resonance near the erbium emission wavelength, i.e., for the apertures with  $R = 193 \text{ nm}$ . As we

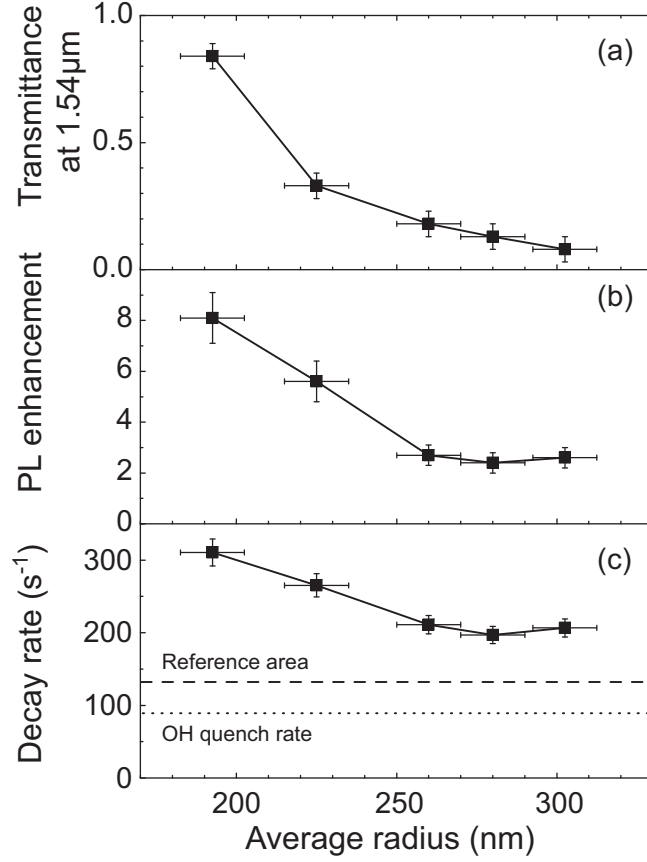


**Figure 2.3:** Transmission and reflection (inset) spectra for the annular aperture arrays. The arrays show large transmission at the resonance wavelength. By increasing the average radius of the annular apertures this resonance wavelength is shifted. The pump wavelength (488 nm) in PL experiments is indicated by an arrow.

increase  $R$  the resonance wavelength increases, shifting away from the Er emission wavelength (see Fig. 2.3(a)), and the PL enhancement decreases, demonstrating a strong correlation between the PL enhancement and cavity resonance condition.

To investigate the origin of the observed trend in the PL enhancement for decreasing  $R$ , we performed time-resolved measurements of the PL decay. For the apertures with a resonance near 1.6  $\mu\text{m}$  ( $R = 193$  nm) and the ones with a resonance the furthest away from the erbium emission wavelength ( $R = 303$  nm) the decay curves are plotted in Fig. 2.4(b). Single-exponential functions are fitted to the curves to obtain a first-order estimate of the decay rate of Er in the various nanocavities. The fitted decay rates for all arrays are plotted in Fig. 2.3(c). We find that the total decay rate for the resonant array with  $R = 193$  nm ( $\Gamma = 311$  s $^{-1}$ ,  $\tau = 3.2$  ms) is 1.5 times as large as that for apertures with  $R = 303$  nm ( $\Gamma = 207$  s $^{-1}$ ,  $\tau = 4.8$  ms). The decay rate for Er in the reference area is  $\Gamma = 132$  s $^{-1}$  ( $\tau = 7.6$  ms), shown as the dashed line in Fig. 2.3(c). Accordingly, the total decay rate of Er for the resonant apertures is increased by a factor 2.4 as compared to that of Er in the reference area.

The corresponding trends in PL intensity and decay rate with varying  $R$  are a strong indication that the observed increase of the PL intensity as the resonance is tuned to the Er transition is related to an increase of the radiative decay rate. As the PL experiments were performed in the linear pumping regime, the increase in PL enhancement from 2.5 for apertures with large radii to 8.1 for the apertures with  $R = 193$  nm indicates that the luminescence quantum efficiency is

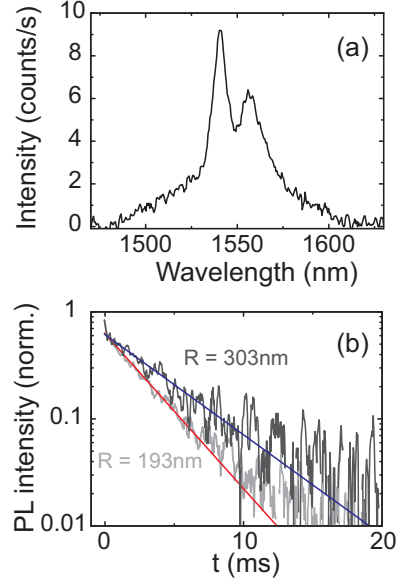


**Figure 2.4:** (a) Erbium luminescence spectrum taken on a planar  $\text{SiO}_2$  film ( $\lambda_{\text{pump}} = 488$  nm) and (b) decay curves for two different annular aperture arrays with a resonance near the erbium emission wavelength ( $R = 193$  nm) and with a resonance the furthest away from  $1.5 \mu\text{m}$  ( $R = 303$  nm).

increased by a factor 3 as we tune the resonance wavelength to the Er emission wavelength. We exclude a difference in pump rate for the various aperture arrays as an alternative cause for the trend observed in the PL intensity. The pump wavelength is much smaller than the resonance wavelength and we observe no change in the transmission near 488 nm for the various aperture arrays (see arrow in Fig. 2.2). It is nonetheless possible that the pump intensity is enhanced for all structures compared to the pump rate in the reference area without Au. Because the magnitude of this effect is unknown, it is not straightforward to quantitatively compare the decay rate enhancement and the PL enhancement.

We can however estimate an upper bound to the enhancement of the radiative rate when the structure is tuned to resonance. The total decay rate  $\Gamma$  is composed of radiative and non-radiative components. There are two sources for non-radiative decay: quenching by OH impurities in the glass, [4] which is independent of the dielectric environment, [23] and absorption by the Au. The OH quench rate, derived from a comparison of the measured decay rate of Er in the reference area, the known radiative decay rate in bulk  $\text{SiO}_2$  ( $54 \text{ s}^{-1}$ ), [24] and the known relative local density of states at the depth of the Er ions in the reference area, [25] amounts to  $\Gamma_{\text{OH}} = 89 \text{ s}^{-1}$  (dotted line in Fig. 2.3(c)). Correcting for the LDOS-independent OH quenching, the remaining decay rate, i.e.,  $\Gamma - \Gamma_{\text{OH}}$ , for the apertures resonant near the Er transition wavelength is increased by a factor 4.1 as compared to the radiative decay rate in bulk  $\text{SiO}_2$ . Taking into account the refractive index of  $\text{SiO}_2$ , the remaining decay rate is thus enhanced by a factor 6 with respect to the decay rate in vacuum. This number constitutes an upper limit to the enhancement of the radiative rate, if the absorption by Au is negligible compared to the power radiated to the far field by the aperture mode.

The quality factor derived from the reflectance data is  $Q = 5.2$  for the array with  $R = 193$  nm. To make a first estimate of the expected Purcell factor  $F$  we take the mode volume equal to the geometrical volume ( $1.3 \times 10^{-2} \mu\text{m}^3$ ), and find  $F = 135$  for these annular apertures. The experimentally derived rate enhancement of a factor 6 is much smaller than the estimate of the Purcell factor. The difference suggests that the coupling of Er to the nanocavity mode is less than optimal. It could be partly due to a possible spatial mismatch between the Er distribution and the

$TE_{11}$  mode profile, and to a distribution in orientation of the Er emission dipole. Moreover, the effective mode volume could differ significantly from the geometrical volume. [26, 27]

More insight in the coupling between emitters and the nanocavity mode could be gained in further experiments, by considering the ensemble distribution of decay rates, the spatial overlap between the cavity mode profile and the Er distribution and the variation in coupling ratio to modes other than the  $TE_{11}$  mode, for off-resonant arrays.

In summary, we have shown that the spontaneous emission decay rate of  $Er^{3+}$  ions at  $1.54\ \mu m$  is controlled using annular apertures fabricated in a Au film. An increased decay rate and PL intensity are observed for apertures filled with Er-doped  $SiO_2$  in a Au film when the localized plasmon resonance of the apertures is tuned to the Er emission wavelength. A 2.4-fold decay rate enhancement and a 8-fold intensity enhancement are observed. The various decay processes and their effects on the decay rate and PL intensity were discussed.

The authors thank Chris Rétif for assistance in fabricating the annular apertures and Simon Huisman and Willem Vos for the use of the set-up for reflection measurements. This work is part of the Joint Solar Programme (JSP) of the “Stichting voor Fundamenteel Onderzoek der Materie (FOM)”, which is financially supported by the “Nederlandse organisatie voor Wetenschappelijk Onderzoek (NWO)”. The JSP is cofinanced by gebied Chemische Wetenschappen of NWO and Stichting Shell Research.

## Chapter 3

# Localized resonance in annular apertures

### 3.1 Introduction

Control of spontaneous emission can be achieved by modifying the local density of optical states (LDOS). In the case of annular apertures the local density of states can be modified by exploiting a localized resonance. In this chapter we want to confirm the existence of this resonance as well as its tunability. To be able to compare the effects on the spontaneous emission for annular apertures of various dimensions we want to tune the resonance wavelength near the Er transition wavelength.

An annular aperture can support multiple plasmonic resonances. The localized resonance that we want to exploit is due to cutoff of the  $TE_{11}$  mode of a coaxial waveguide. At cutoff the wavevector of a wave propagating along the aperture becomes close to zero such that the phase is constant. As in a Fabry-Perot etalon the wave propagating in one direction constructively interferes with the reflected wave propagating in the opposite direction, resulting in an enhanced electromagnetic field.

### 3.2 Controlling spontaneous emission

The spontaneous emission is related to the local density of states via Fermi's golden rule

$$\Gamma = \frac{2\pi}{\hbar} |\langle f | H | i \rangle|^2 \rho(\vec{x}, \omega) \quad (3.1)$$

where  $\rho$  is the local density of states and  $\langle f | H | i \rangle$  is a coupling term. [1] We can enhance the spontaneous emission decay rate by exploiting the localized resonance in annular apertures to increase the local density of states. Our interest is in increasing the radiative decay rate as distinguished from increasing the non-radiative decay rate. It is well known that annular apertures couple strongly to far field radiation, since they can assist very large transmission through a metal film. [13–15]

It is not straightforward to calculate the enhanced local density of states. It is easier to find the solution of Maxwell's equations for the annular apertures upon illumination with a plane wave, calculating the enhancement of the electromagnetic field. This field enhancement suggests that the local density of optical states (LDOS) at the resonance wavelength is also enhanced. Reciprocity states that the radiated power of a dipole in a photonic system is equal to the power absorbed by the dipole when the system is illuminated from all angles. In the case of a cavity this illumination may be enhanced inside the cavity, resulting in increased absorption by the dipole. Accordingly, the local density of states in the cavity is increased, as that scales by the power radiated by an emitting dipole. This reciprocity argument is only valid if the angles of illumination and radiation are the same. In the case of annular apertures, however, it has been shown that the excitation of the mode is angle-independent. [28, 29] This allows us to calculate the enhancement by illuminating

the cavity with a single plane wave, the result of which indicates whether or not the local density of states is enhanced at specific positions and frequencies.

### 3.3 Finite difference time domain simulations

One of the techniques to find the solution of Maxwell's equations are so-called finite difference time domain (FDTD) simulations. FDTD is a marching-in-time procedure that simulates the electromagnetic waves in a finite region. This region is meshed into a number of small volumes and for each volume the electromagnetic field is calculated at discrete times. The time steps are typically of the order of femtoseconds and the spatial meshing typically uses a subwavelength resolution with 10 to 20 samples per wavelength.

We employ FDTD to confirm the existence of the localized resonance as well as its tunability in annular apertures. Annular apertures in a metal exhibit high transmission due to this localized resonance. [13, 14] Therefore, the resonance wavelength can be determined from the peak transmission wavelength. This allows us to determine the the annular apertures' optimal shape for controlling the spontaneous emission of  $\text{Er}^{3+}$ .

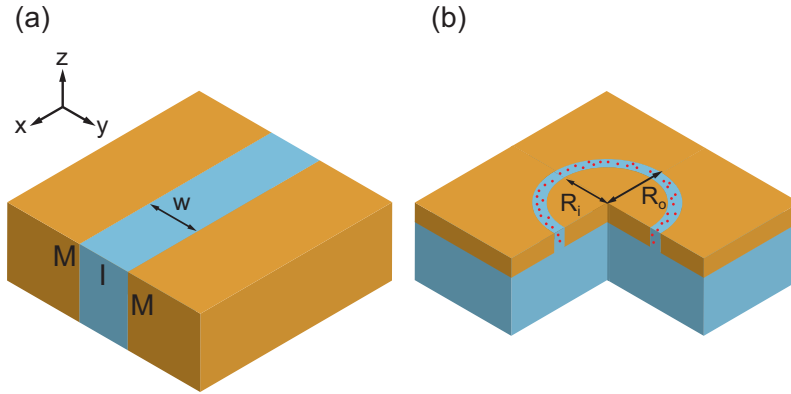


**Figure 3.1:** Schematic of (a) a MIM slab waveguide and (b) a single annular aperture in metal.

The resonance wavelength or cutoff condition can be deduced from the geometry of the annular apertures. It is instructive to first look at a metal-insulator-metal (MIM) slab waveguide, as depicted in Fig. 3.1(a). The waveguide is infinitely long in the  $x$ -direction. We consider SPP propagation in the  $x$ -direction, i.e.,  $k_z = 0$ . For this mode an effective index of refraction can be defined as  $n_{eff} = k_x/k_0$ .

Now consider a rolled-up MIM waveguide, i.e., an insulator filled annular aperture in a metal film, as depicted in Fig. 3.1(b), with SPP waves travelling around the circumference. This view is completely analogous to the interpretation of cutoff of a wave in the  $z$ -direction, as both are characterized by  $k_z = 0$ . The cylindrical geometry allows stable modes when the wavelength of the surface plasmons is a half integer times the average circumference of the annular aperture. This means that  $\lambda_{SPP} = \pi(R_i + R_o)$ , where  $R_i$  and  $R_o$  are the inner and outer radius of the aperture, respectively.

As a result the cutoff condition is approximated by

$$\lambda = n_{eff} (R_i + R_o) \pi \quad (3.2)$$

The resonance wavelength is proportional to the average radius. For large widths,  $n_{eff}$  is close to the refractive index of the dielectric inside the apertures. For small widths, however, the skin depth of the mode will decrease, [30] i.e., the imaginary part of  $k_y$  increases. Due to the wave equation  $k^2 = k_x^2 + k_y^2$ , such that an increase in  $\text{Im}(k_y)$  causes an increase in  $\text{Re}(k_x)$ . This in turn means that the effective index of refraction is increased. Therefore, the resonance wavelength will increase for decreasing width and vice versa.

### 3.3.1 Experimental

We use the commercially available software FDTD solutions by Lumerical in which a plane wave illuminating a hexagonal array of annular apertures is simulated. For our experiments we want to create close-packed aperture arrays to get a high Er fill fraction. The apertures are embedded in a Au film and filled with SiO<sub>2</sub>. To model the Au film we use experimental data of the dielectric constants as measured by Johnson and Christy. [31] In the wavelength range of interest this data is fitted to a model with 5 fit parameters which is either a conductive model, a plasma model, the Debye model or the Lorentz model. [32] For the SiO<sub>2</sub> ring and substrate we use a fixed refractive index of 1.53.

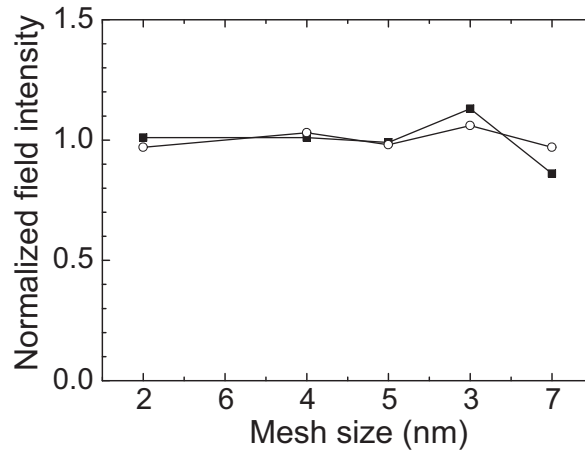


**Figure 3.2:** Typical convergence for the electric field intensity at a depth of 50 nm in the SiO<sub>2</sub> ring. Data for the full squares is recorded 10 nm from the inner Au core and for the open circles in the middle of the SiO<sub>2</sub> ring.

The annular apertures are illuminated by a chirped plane wave with accompanying wavelengths ranging from  $\sim 400$  nm to  $\sim 3$   $\mu$ m. The simulations have a mesh size of 5 nm in the vicinity of the apertures and 14 nm elsewhere. This mesh size is chosen to make sure that the recorded fields converge, i.e., that they do not change when using a smaller mesh size, as seen in Fig. 3.2.

In the simulations we record both the transmitted and reflected field at the simulation boundaries as well as the electric field intensity in a cross-cut of the apertures.

### 3.3.2 Results

For an annular aperture with an average radius of 193 nm and a width of 105 nm the transmission along with field intensity in the aperture is shown in Fig. 3.3(a). The field intensity is recorded at a depth of 50 nm and a distance of roughly 20 nm from the inner Au core. The arrows indicate Rayleigh anomalies, the solid ones at the glass interface and the dashed one at the air interface. The corresponding periodicity of the array is 903 nm. It can be seen that there is a resonance at about 1810 nm agreeing with Eq. 3.2 according to which the resonance wavelength is 1814 nm. This confirms the existence of the localized resonance and its interpretation as cutoff of a waveguide mode. It also shows us that the phase shifts at the Au/Air and Au/SiO<sub>2</sub> interfaces are zero and that the difference in skin depth between Au and a perfect electric conductor is negligible for this particular geometry.

Fig. 3.3(b) shows the transmission spectrum, reflection spectrum and the calculated absorption spectrum,  $A = 1 - R - T$ . We observe no difference in wavelength between the peak in transmission and dip in reflection. Accordingly, the Fano effect plays no role for this specific geometry as it would cause a difference in peak wavelength due interference of a resonant (direct scattering) and

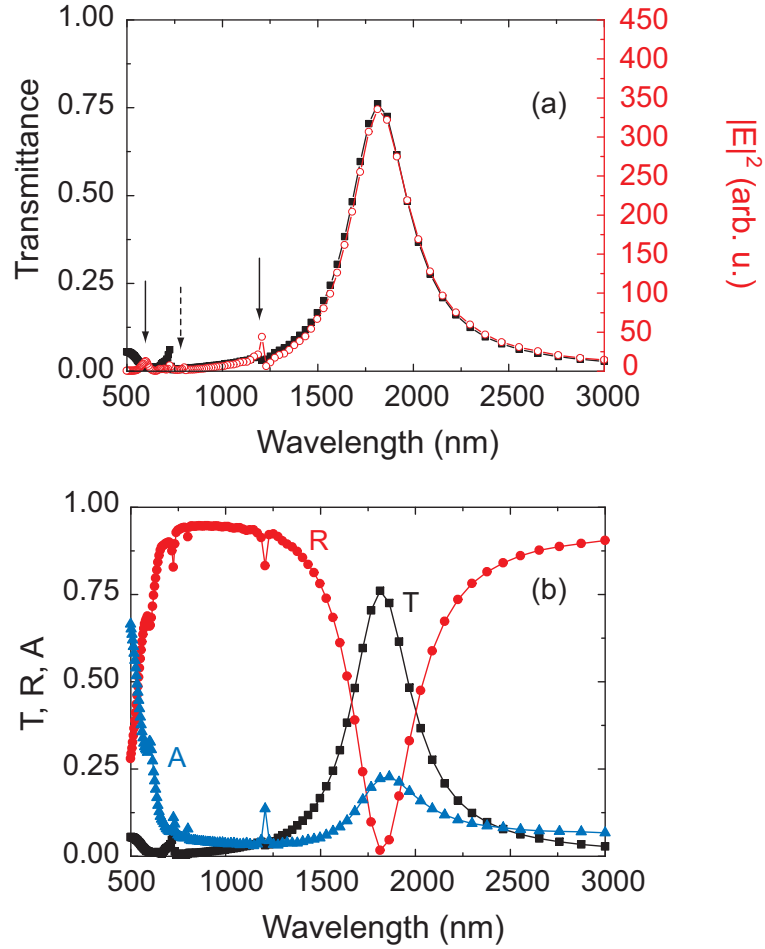


**Figure 3.3:** Transmission along with either electric field intensity (a) or reflection and absorption (b) of SiO<sub>2</sub>-filled annular aperture arrays in Au, with  $R = 193$  nm and  $w = 105$  nm. The periodicity of the array is 903 nm. The field intensity is recorded at a depth of 50 nm and a distance of roughly 20 nm from the inner Au core. The arrows indicate Rayleigh anomalies, the solid ones at the glass interface and the dashed one at the air interface.

non-resonant (surface plasmon excitation) channel. [33] The relatively high absorption near 500 nm is due to absorption of light by the Au film.

A 2D map of the electric field at the resonance frequency is depicted in Fig. 3.4. For this particular geometry the electric field is enhanced up to a factor 200 in the annular apertures and we expect an increase of the local density of optical states at 1.8  $\mu\text{m}$  of the same order of magnitude.

The resonance wavelength can be tuned by modifying the width or radii of the annular apertures. To confirm this tunability we first simulate a number of different aperture arrays in which we keep the width of the apertures constant at 100 nm and increase the outer and inner radius from 150 to 250 nm respectively 50 to 150 nm. According to Eq. 3.2 the resonance wavelength should linearly increase for the increasing radii. We observe that the resonance wavelength indeed behaves as predicted, see Fig. 3.5(a). By increasing the average radius we can tune the resonance over a wavelength range of 1  $\mu\text{m}$ . Geometries with varying width and either a varying outer or inner radius are also simulated. The results for a fixed outer radius are depicted in Fig. 3.5(b). In this case the

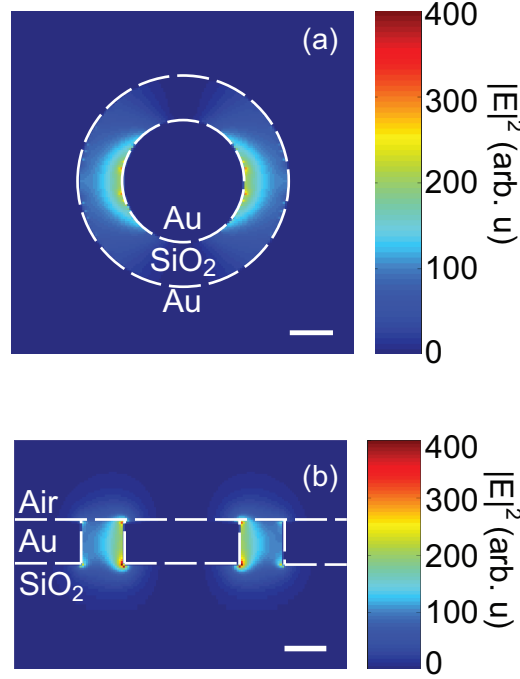


**Figure 3.4:** Electric field intensity in SiO<sub>2</sub>-filled annular apertures in Au: (a) top view, data at a depth of 50 nm; (b) side view, data along the symmetry axis. The polarization is horizontal and the scalebars are 100 nm.

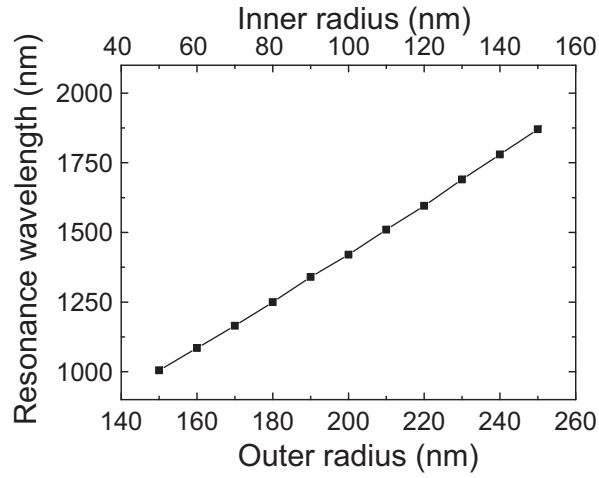
change in both width and inner radius cause the resonance wavelength to increase. The increase of the derivative to  $R_o$  or  $w$  of the resonance wavelength is expected to be due to confinement as increasing  $R_i + R_o$  can only explain a linear increase of the resonance wavelength. If the inner radius is kept constant and both the width and outer radius are increased their effect on the resonance wavelength will be opposite. An increasing width would cause the resonance wavelength to decrease while an increasing outer radius would cause the resonance wavelength to increase. We observe both these effects in Fig. 3.5(c) where the resonance wavelength first decreases and then increases as the width and outer radius are increased.

The Purcell factor is given by

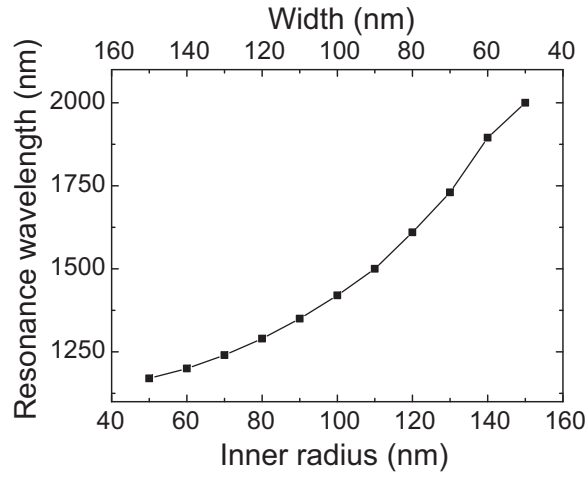
$$F = \frac{3\lambda_0^3 Q}{4\pi^2 V}. \quad (3.3)$$

To make a first estimate of the expected Purcell factor  $F$  we take the mode volume equal to the geometrical volume for the various aperture arrays. The quality factor can be determined from the simulated transmission spectra. The resulting quality and Purcell factors for the various aperture arrays are depicted in Fig. 3.6. The Purcell factor seems to be mostly determined by the resonance wavelength and modal volume. The quality factor hardly changes for the various arrays, while the resonance wavelength and volume do.

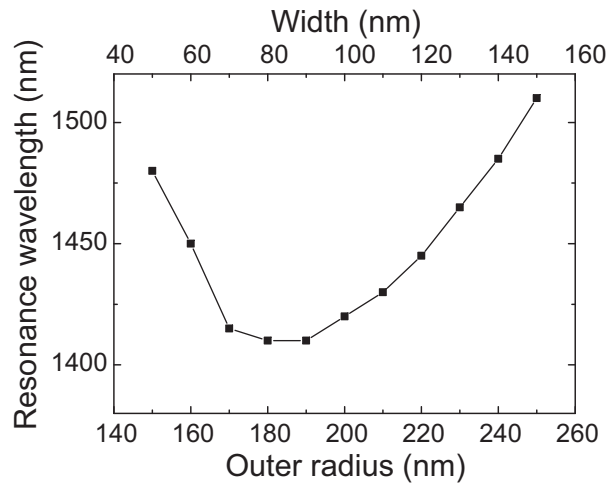
The tunability of the resonance wavelength allows us to compare the effects on the spontaneous emission of Er for annular apertures of various dimensions. The enhanced local density of states is expected to cause an increased radiative decay rate. Therefore, it is preferable to keep the non-radiative decay rate constant. The most important contributions to the non-radiative decay are OH-quenching and quenching to the metal film. The former will be constant over the entire sample, but the latter can be influenced by the proximity of Er ions to the metal film. Therefore, we keep the width of the apertures constant in the experiment so this proximity to the metal is kept constant as well. Varying the average radius will then allows us to linearly tune the resonance wavelength.



(a) Resonance wavelength as a function of inner and outer radius. The dielectric width is fixed at 100 nm.

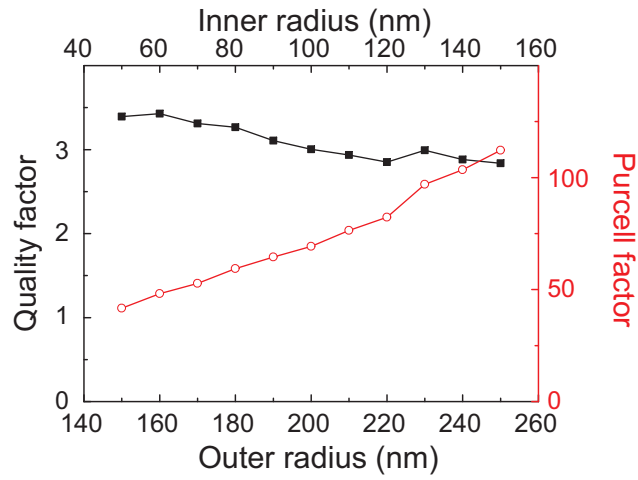


(b) Resonance wavelength as a function of inner radius and width. The outer radius is fixed at 200 nm.

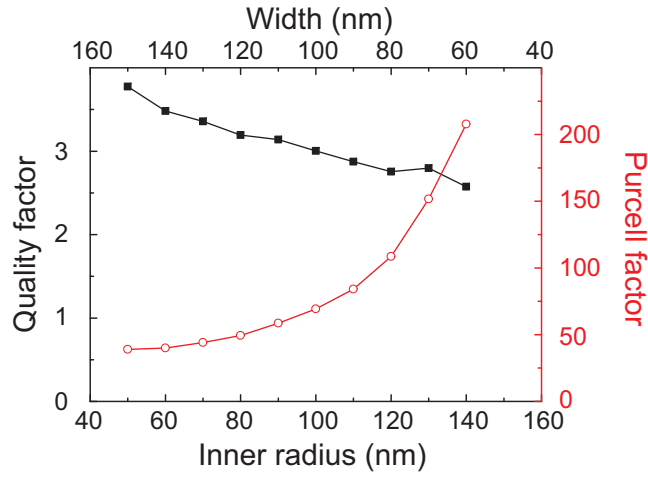


(c) Resonance wavelength as a function of outer radius and width. The inner radius is fixed at 100 nm.

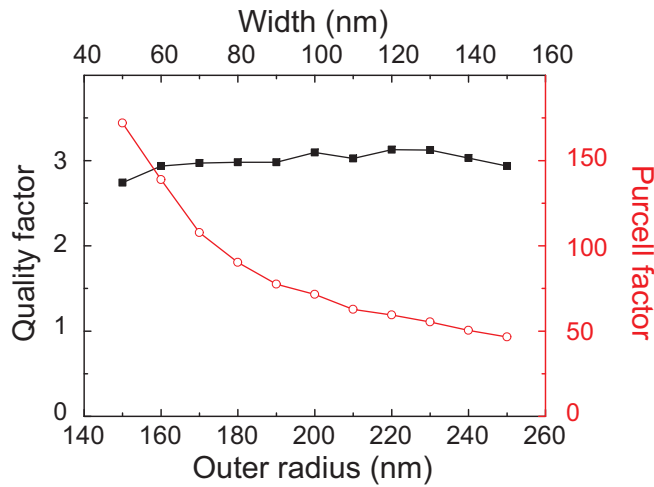
**Figure 3.5:** Resonance wavelength for different series of aperture dimensions.



(a)  $Q$  and  $F$  as a function of inner and outer radius. The dielectric width is fixed at 100 nm.



(b)  $Q$  and  $F$  as a function of inner radius and width. The outer radius is fixed at 200 nm.



(c)  $Q$  and  $F$  as a function of outer radius and width. The inner radius is fixed at 100 nm.

**Figure 3.6:** Quality factor ( $Q$ ) and Purcell factor ( $F$ ) for different series of aperture dimensions.

### 3.4 Rayleigh-Wood anomalies

As the apertures in the arrays are periodically arranged the array also exhibits resonances that are related to grating diffraction. These so-called Wood anomalies are due to the coupling of incident light to surface plasmons propagating along the SiO<sub>2</sub>/Au or Au/Air interface. As a result of the momentum mismatch between photons and plasmons at the same frequency it is not possible for incident light to directly couple to surface plasmons. The surface plasmons have a larger wavevector for a given frequency than photons. In case of a periodic structure the momentum necessary to excite the surface plasmons can be supplied by the incident photon momentum parallel to the surface and by the reciprocal array vectors. For a hexagonal array with spacing  $a$  the surface plasmon (SP) momentum is given by

$$\vec{k}_{SP} = \vec{k}_{//} + (N_1 \vec{e}_1 + N_2 \vec{e}_2) \frac{4\pi}{a\sqrt{3}} \quad (3.4)$$

where  $N_1$  and  $N_2$  are integers,  $\vec{k}_{//}$  is the component of the wavevector parallel to the interface and  $\vec{e}_i$  are the unit vectors along the unit cell. [34] This is the condition for Wood's anomalies. As we do not know the surface plasmon dispersion relation we approximate  $k_{SP}$  with  $nk_0$ , which is the condition for Rayleigh anomalies. Taking  $k_{SP} = nk_0$  Eq. 3.4 leads to

$$\lambda = \frac{a\sqrt{3}}{2\pi m} (n - \sin \theta) \quad (3.5)$$

where  $m$  is an integer and  $\theta$  is the angle of incidence of the photon. In Fig. 3.3 the Rayleigh anomalies are indicated with arrows. In the simulations and experiment the periodicity of the arrays is chosen such that the Rayleigh anomalies are all at wavelengths much smaller than the Er transition wavelength.

While it is possible for Rayleigh-Wood anomalies to modify spontaneous emission, e.g., by causing the emission to be directional, this is not related to the Purcell effect. The Purcell effect concerns a cavity with a certain quality factor and volume.

### 3.5 Conclusion

We have shown in simulations that annular apertures indeed exhibit a localized resonance. The electromagnetic field is enhanced inside the apertures resulting in an enhanced local density of states at the resonance wavelength. To obtain the maximum possible mode overlap with the resonant TE<sub>11</sub> mode and the Er ions we need to selectively position the ions inside the SiO<sub>2</sub> annular structures.

Annular aperture arrays also exhibit grating resonances where incident light couples to surface plasmons propagating along the SiO<sub>2</sub>/Au interface or the Au/Air interface. As we are interested solely in the localized resonance we have to make sure that the periodicity is chosen such that there are no Rayleigh-Wood anomalies near the Er transition wavelength of 1.54  $\mu\text{m}$ .

## Chapter 4

# Fabrication of Er-filled annular apertures in a metal film

### 4.1 Introduction

There are a number of different techniques that offer the possibility of nanoscale fabrication. Two often used methods are focused ion beam (FIB) and electron beam lithography (EBL). Both of these allow for the fabrication of diverse structures at high resolution. As we need to selectively position the Er ions in the annular apertures we will use electron beam lithography to create the SiO<sub>2</sub>-filled annular apertures. Combined with reactive ion etching (RIE) this allows us to remove parts of a substrate in order to create SiO<sub>2</sub> rings which we can then embed in a Au film.

### 4.2 Fabrication steps

In an EBL process a substrate is covered with a layer of either negative or positive resist parts of which will be exposed to an electron beam. By developing the resist layer either the exposed (positive resist) or non-exposed (negative resist) areas are selectively removed. This pattern can then be transferred to an evaporated layer or the substrate itself. For our purposes we employ EBL with a negative resist by exposing annular areas in the resist layer. The pattern is transferred to the substrate using reactive ion etching (RIE) and a Au layer is evaporated onto the substrate through the same resist mask. As a final step lift-off is used to remove the excess Au and resist such that we end up with annular apertures in a Au film filled with Er doped SiO<sub>2</sub>.

A fused silica (Heraeus Suprasil 300) substrate is first doped with erbium by 150 keV Er<sup>+</sup> ion implantation at normal incidence using a fluence of  $3.0 \times 10^{14} \text{ cm}^{-2}$ . This results in a distribution of Er ions at a mean depth of 82 nm with a standard deviation of 18 nm, as calculated with the Monte Carlo program SRIM. [21] The peak Er concentration is 0.29 at. %. The sample is then annealed for one hour in a rapid thermal annealer (RTA) at 900°C in an Ar atmosphere to activate the Er ions and remove implantation related defects. [35] Subsequently the sample is cleaned in a 1:1:5 solution of NH<sub>4</sub>OH + H<sub>2</sub>O<sub>2</sub> + H<sub>2</sub>O.

The rest of the process is schematically depicted in Fig. 4.1. To obtain maximum mode overlap of the Er ions with the TE<sub>11</sub> mode the emitters will be positioned in annular apertures in a 100 nm Au film. Therefore, the mean depth of Er is reduced to 50 nm by removing the top 30 nm of the substrate with reactive ion etching. This not only causes the mean depth of Er to be at the middle of the Au film, but also makes sure that there will be no Er ions beneath the film.

The substrate is then again cleaned in a 1:1:5 solution of NH<sub>4</sub>OH + H<sub>2</sub>O<sub>2</sub> + H<sub>2</sub>O, after which we deposit a layer of polymethylmethacrylate (PMMA) by spin-coating a solution of 8% in anisole (495k) at 750 rpm for 5 s and then at 4000 rpm for 45 s. This results in a layer of 490 nm when baked for 15 minutes at 175°C. On top of the PMMA a 20 nm thick Ge layer is sputtercoated and baked at 115°C for 5 minutes. Next, we spincoat about 10 nm of hexamethyldisilazane (HDMS) primer at 4000 RPM for 45 s and bake the sample at 115°C for 1 minute. As a final layer we

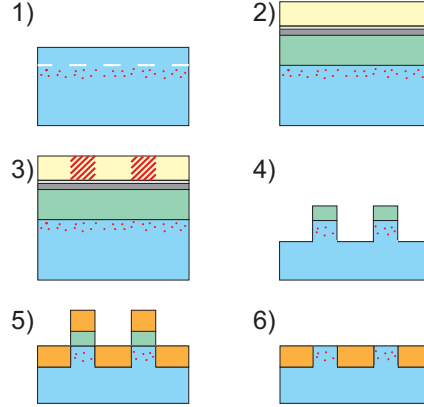


**Figure 4.1:** Electron beam lithography process using a negative resist. The steps are 1) etching through top layer of the substrate, 2) depositing resist stack, 3) e-beam exposure, 4) etching through resist stack and part of substrate, 5) gold evaporation and 6) lift-off.

spincoat roughly 50 nm of Ma-N 2401 at 750 rpm for 5 s followed by 6000 rpm for 45 s and bake that again at 115°C for 3 minutes.

The sample is then exposed to a 20 kV electron beam using a Raith e\_LiNE to pattern annular structures, at doses of 60 and 120  $\mu\text{C}/\text{cm}^2$ . These structures are patterned on both sides of the sample. The negative resist is developed in Ma-D532 and cleansed with deionized water. This results in annular structures in the resist. These structures are transferred to the layers beneath by reactive ion etching. First, the primer and Ge layers are removed by etching with a  $\text{SF}_6/\text{O}_2$  plasma etch. As an intermediate step the RIE chamber is cleaned with an  $\text{O}_2$  plasma for 2 hours to avoid modification of the resist sidewalls by impurities. Next, the PMMA layer is removed with a  $\text{O}_2$  plasma etch. Finally, we remove 100 nm of  $\text{SiO}_2$  with a  $\text{CF}_3/\text{Ar}$  plasma etch. At this point we have annular structures in the  $\text{SiO}_2$  substrate that are still covered by PMMA.

We then evaporate 100 nm of Au over one half of the sample, such that one set of structures is embedded in Au while the other one is not. This is done to later obtain structures that serve as reference to the annular apertures in Au. Finally, we remove the excess Au and PMMA in a lift-off step. By submerging the sample in 1-methyl-2-pyrrolidone (NMP) at 60°C for 17 hours the PMMA is dissolved. To make sure that all the PMMA and excess Au are removed we sonicate the sample for a few seconds. This results in either Er: $\text{SiO}_2$  filled annular apertures in a Au film or Er: $\text{SiO}_2$  rings. SEM images of both the annular apertures and rings are depicted in Fig. 4.2.

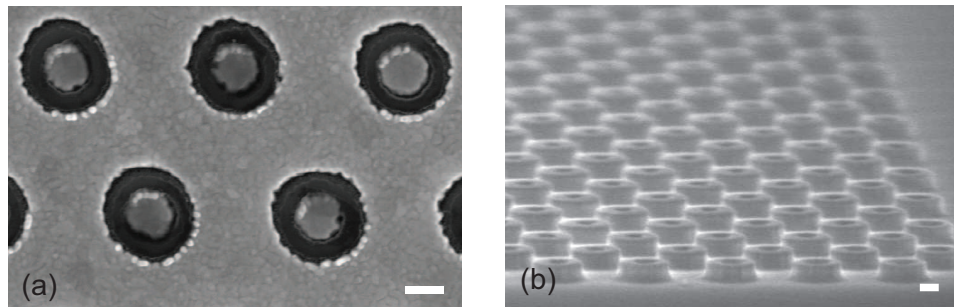


**Figure 4.2:** SEM images of annular structures: (a) Er: $\text{SiO}_2$ -filled annular apertures in a Au film on top of  $\text{SiO}_2$ ; (b) Er: $\text{SiO}_2$  on top of  $\text{SiO}_2$ . The scalebars are 200 nm.

The annular structures are arranged in  $50 \times 50 \mu\text{m}^2$  hexagonally ordered arrays, see Fig. 4.3 for an example. Two different series of these arrays are fabricated. For each series we vary the average radius,  $R = (R_o + R_i)/2$ , for the apertures in the different arrays. At the same time we try

to keep the width constant to maintain a constant average distance of Er ions to the metal surface, and therefore a constant rate of direct quenching to the metal of excited Er. In doing so we can tune the resonance wavelength solely by increasing the average radius and thus linearly increase the resonance wavelength. Moreover, the periodicity is varied such that the total amount of Er ions is the same in all arrays.

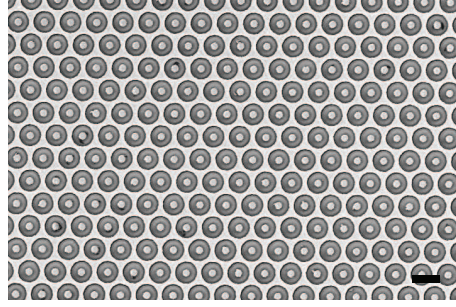


**Figure 4.3:** SEM image of an array of annular apertures. The scalebar is 1  $\mu\text{m}$ .

### 4.3 Lift-off

The success rate of the lift-off step is quite dependent on the exact parameters of the resist stack. If the PMMA layer is too thin lift-off will not succeed and there will be Au rings left on top of the annular apertures. An example of this effect is shown in Fig. 4.4. A thick PMMA layer will, however, result in a low resolution. Therefore, there is an optimal layer thickness such that lift-off will succeed and we are still able to obtain a high resolution.

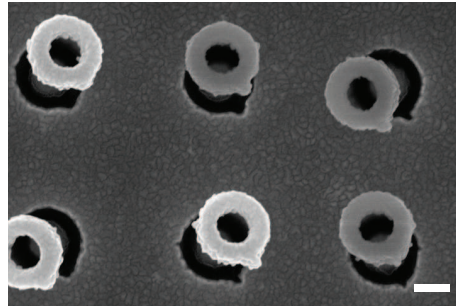


**Figure 4.4:** SEM image of annular apertures for which lift-off did not succeed. The scalebar is 200 nm.

Even though the final etch step is targeted at  $\text{SiO}_2$  it also affects the PMMA layer, which influence the lift-off. Moreover, the Ge mask is removed during the  $\text{SiO}_2$  etch. We therefore measured the etch rates in  $\text{SiO}_2$  and PMMA and found them to be 55 nm/minute and 31 nm/minute, respectively. As we expect the etch rate of nanoscale PMMA structures to be different from its bulk value it is not possible to accurately predict the thickness of the PMMA covering the annular structures in  $\text{SiO}_2$ , i.e., the thickness of the PMMA layer just before Au evaporation. It is this thickness that determines whether or not lift-off will succeed as for thin layers the gold film on silica may be connected to the gold covering the PMMA.

## 4.4 Conclusion

Using a process of electron beam lithography and reactive ion etching we are able to fabricate Er:SiO<sub>2</sub> filled annular apertures in a Au film. The apertures are arranged in two different series of hexagonal arrays in which the width is kept constant and the average radius of the annular apertures is varied to tune the resonance wavelength.

## Chapter 5

# Spontaneous emission of Er in nanocavities

### 5.1 Introduction

It is not straightforward to measure the radiative decay rate of an emitter, but it is possible to deduce whether or not the radiative rate has been modified by measuring the total decay rate and photoluminescence intensity. An increased radiative rate would cause both the total decay rate as well as the PL intensity to increase, as it can lead to an increase of the quantum efficiency. In Chapter 3 we concluded that we expect the local density of optical states (LDOS) at the resonance wavelength to be enhanced in the annular apertures. In Chapter 2 we argued that when this resonance is tuned to the Er transition wavelength the localized resonance leads to an increased radiative decay rate of Er ions. This tuning of the resonance wavelength can be determined from transmission measurements.

In this chapter we will describe the set-ups used for the various measurements and discuss results for a series of annular apertures different from the one described in Chapter 2.

### 5.2 Experimental

#### 5.2.1 Transmission

Transmission spectra of the arrays are obtained by illuminating the sample with an Ando halogen white light source from the air side of the sample with a numerical aperture (NA) of 0.02 and collecting the transmitted light through a 0.75 NA objective. This means that the sample is illuminated by a beam with only a small number of different wavevectors, i.e., different incident angles, and that the beam is focused to a relatively large spot. In this case the illumination spot size is roughly  $50 \times 50 \mu\text{m}^2$ . As we use an objective with high NA most angles will be detected, but the spot size will be much smaller. This detection spot size is roughly  $8 \times 8 \mu\text{m}^2$ . One of the key properties of a localized resonance is that the angle of incidence is irrelevant for the excitation of the resonance. [28, 29] The fact that the resonance is localized also means that the transmission through a single aperture will be equal to that of an ensemble of apertures with the exception of the introduced resonances due to grating diffraction and a possible shift in resonance wavelength due to coupling. Accordingly, the NA of the incident beam mostly affects the observation of grating resonances, which will broaden for larger NAs as the number of different angles of incidence increases. The collected light is coupled into a  $100 \mu\text{m}$  core fiber that is connected to a spectrometer. The light is then detected with either a Si CCD for visible wavelengths or an InGaAs diode array for infrared light. This allows us to measure the transmission in a wavelength range from 400 to 1600 nm. The set-up is depicted in Fig. 5.1.

As the spectral detection range of the transmission set-up is limited to  $1.6 \mu\text{m}$  we use a different set-up which can measure reflection up to  $2.4 \mu\text{m}$  to confirm that the resonance shifts. The high

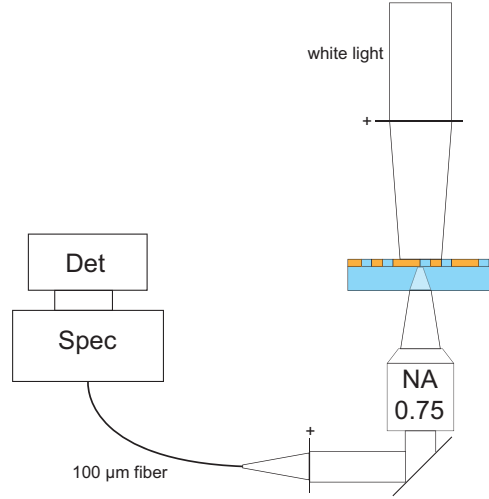


**Figure 5.1:** Set-up for the transmission measurements. The sample is illuminated from the air side by an Ando halogen white light source at normal incident angle through a 0.02 NA lens. The light is collected with a 0.75 NA objective and coupled to a 100  $\mu\text{m}$  core fiber which is connected to a spectrometer with detector.

transmission of the annular apertures is accompanied by a dip in reflection from which it is also possible to determine the resonance wavelength. Reflection spectra are recorded using a 0.65 NA reflective objective and a Biorad FTS6000 Fourier transform spectrometer with an InAs photodiode. The spot size is roughly  $2 \times 2 \mu\text{m}^2$ . The set-up is depicted in Fig. 5.2.

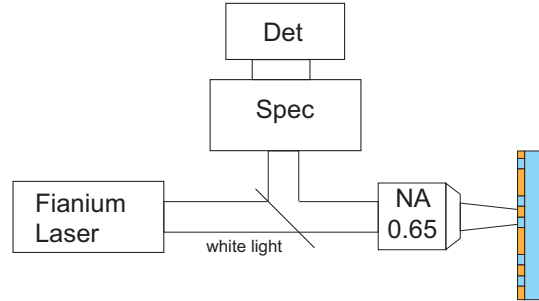


**Figure 5.2:** Set-up for the reflection measurements. The sample is illuminated by a Fianium supercontinuum laser through a 0.65 NA reflective objective. The light is collected through the same objective and passed to a Biorad Fourier transform spectrometer with an InAs photodiode.

### 5.2.2 Photoluminescence

To measure the photoluminescence (PL) of the erbium ions the sample is illuminated with light from an argon ion laser operating at 488 nm incident under a  $22^\circ$  angle to the sample surface from the air side of the metal film. The light is focused to an elliptically shaped Gaussian spot with a full width at half maximum of 34  $\mu\text{m}$  along one direction and 85  $\mu\text{m}$  along the other, as measured using a razor blade. The peak power density is 275  $\text{W}/\text{cm}^2$  for intensity measurements and 680  $\text{W}/\text{cm}^2$

for time-resolved measurements. The 488 nm light excites the  $\text{Er}^{3+}$  ions which can then relax to their ground state by emitting a photon via the  ${}^4\text{I}_{13/2} \rightarrow {}^4\text{I}_{15/2}$  transition at  $1.54 \mu\text{m}$ . We collect this luminescence with a 0.45 NA objective at the air side of the sample. The luminescence is first filtered with a 532 nm long pass filter to eliminate reflected laser light and then passed through either a 1100 nm long pass filter for intensity measurements or a 1500 nm long pass filter for time-resolved measurements. PL intensity is measured with a spectrometer with an InGaAs diode array detector while measurements of the decay rate are performed with a monochromator and North Coast EO-817s Ge detector with a response time of 30  $\mu\text{s}$ . The laser is modulated at 7 Hz with an acousto-optic modulator for these decay rate measurements. The set-up is depicted in Fig. 5.3

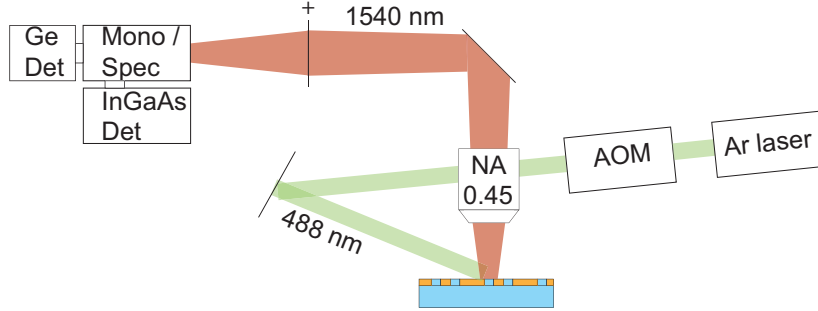


**Figure 5.3:** Set-up for photoluminescence measurements. The sample is illuminated by an Ar laser operating at 488 nm. The light is modulated by an AOM and incident at a  $22^\circ$  angle to the sample surface from the air side. The Er emission at  $1.54 \mu\text{m}$  is collected with a 0.45 NA objective and passed to either a monochromator and Ge detector for time resolved measurements or a spectrometer and InGaAs detector for intensity measurements.

The frequency response of the time resolved measurement set-up is not flat. This means that the measured signal will be deformed resulting, in this case, in what seems like a slow component in the signal decay. The frequency response can be described by an impulse response function  $h(t)$ , such that

$$y(t) = h(t) * x(t) \quad (5.1)$$

where  $x(t)$  is the actual signal decay that we want to measure and  $y(t)$  is the measured signal decay. It is possible to calculate the real signal decay from  $y(t)$  if  $h(t)$  is known. In that case it is also possible to filter the signal in real-time by adding a component with impulse response  $h(t)^{-1}$ .

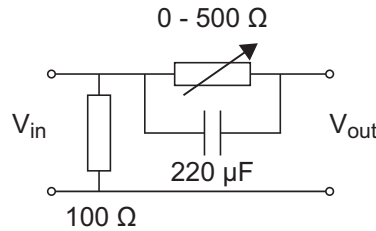


**Figure 5.4:** Electronic circuit of the filter used to correct for the frequency response of our time resolved measurement set-up.

For our system the component needed to correct for the frequency response is a low-pass filter with a flat phase response. The electronic circuit of this is shown in Fig. 5.4. The variable resistance can be used to fine-tune the filter response by modifying the cutoff frequency of the filter. The output of the Ge detector is passed through this filter to an oscilloscope. To test the new impulse response of the system we modulated a diode laser operating at  $1480 \text{ nm}$  with a single exponential decay.

As the lifetime of  $\text{Er}^{3+}$  is typically in the order of 10 ms we tuned the filter such that the measured decay rate corresponds to the modulation input of the laser for lifetimes in the range of 1 to 50 ms.

### 5.3 Results

Two different series of annular aperture arrays with increasing average radius of the apertures were fabricated. Care is taken to keep the width constant at 100 nm for one of the series and at 230 nm for the other. The results for the series with narrow annular apertures are presented in Chapter 2. The results for the wide apertures will be presented here.

#### 5.3.1 Transmission

Transmission spectra for the wide series are shown in Fig. 5.5. For this series we also observe the typical large transmission due to the localized resonance supported by the individual apertures. In this case, the resonance wavelength shifts from values below to values above the Er transition wavelength of 1.54  $\mu\text{m}$ . Again implying a similar effect on the LDOS as argued in Chapter 2.

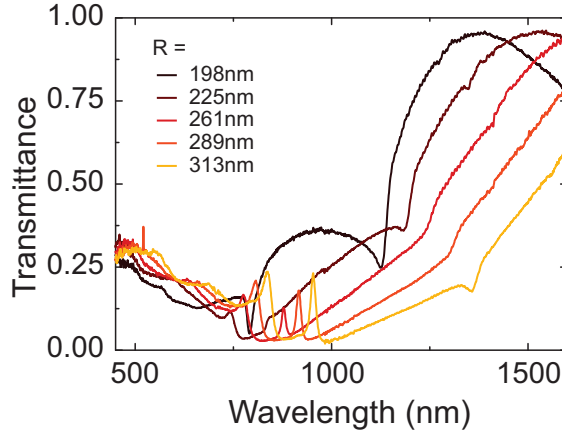


**Figure 5.5:** Transmission spectra for the annular aperture arrays with a width of 230 nm. The arrays show large transmission at the resonance wavelength. By increasing the average radius of the annular apertures this resonance wavelength is shifted.

#### 5.3.2 Photoluminescence

As for the narrow series we measure the PL intensity and decay rate for the wide series. As before, the PL enhancement is taken as the ratio of the PL intensity from Au nanocavities to that from bare silica rings. For both luminescence spectra the background is subtracted and the intensity is integrated from 1450 nm to 1650 nm. The resulting PL enhancement is shown in Fig. 5.6(b). For all the different aperture arrays we observe an increased photoluminescence intensity and the maximum PL enhancement is a factor 3.4 observed for both the array of apertures with  $R = 261$  nm and the one with apertures of  $R = 288$  nm.

We also measure the total decay rate from the series of wide aperture arrays for which we use the same method as described in Chapter 2. The results are shown in Fig. 5.6(c). We observe no significant change in decay rate between the different arrays. Compared to Er in a part of the sample without patterning or Au the decay rate in the wide apertures is on average increased by a factor 1.2.

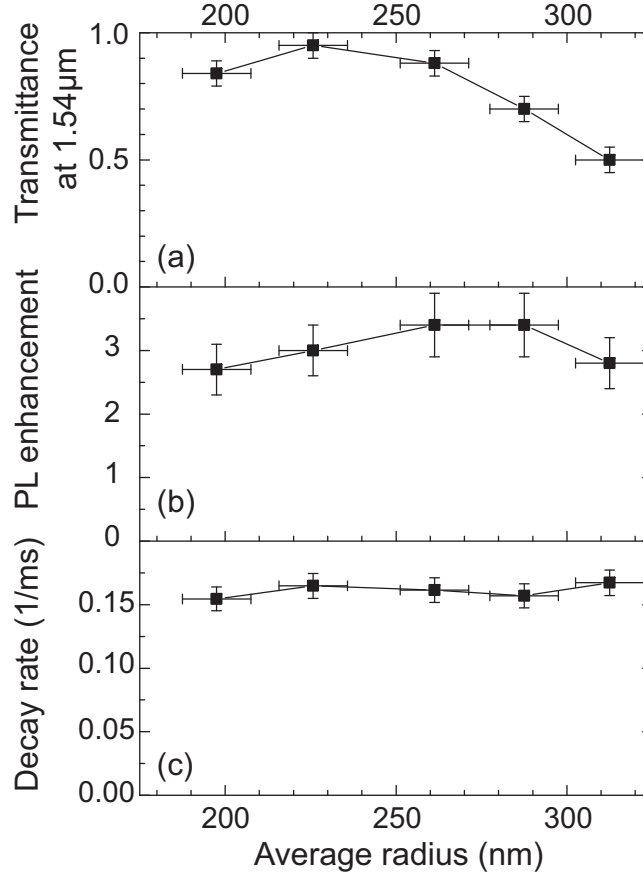


**Figure 5.6:** Optical properties of Er-doped wide annular apertures as a function of average aperture radius  $R$ . (a) Transmittance at 1.54  $\mu\text{m}$ ; (b) PL enhancement compared to similar arrays of silica rings not covered in Au; (c) Er decay rate at 1.54  $\mu\text{m}$ .

## 5.4 Discussion

As the decay rate does not significantly change for the different arrays of 230 nm wide apertures it appears that there is no effect on the radiative decay rate. For the series of narrow apertures we observed both an increased radiative decay and an enhancement of the excitation rate. While the photoluminescence intensity is enhanced for the wide apertures it is likely that this is due to an enhanced pump field resulting in an increased excitation rate.

According to Purcell the maximum decay rate enhancement is given by

$$F = \frac{3\lambda_0^3 Q}{4\pi^2 V}. \quad (5.2)$$

In Chapter 2 we made a first estimate of the expected Purcell factor of  $F = 135$ . The quality factor derived from the transmittance data is  $Q = 2.5$  for the array of wide apertures with  $R = 198$  nm. Their geometrical volume is  $3.05 \times 10^{-2} \mu\text{m}^3$ . Using the same method to make a first estimate of the Purcell factor we find  $F = 15$  for this array. For the narrow apertures we measured a maximum LDOS-dependent decay rate enhancement of 4.1. Taking into account the difference in Purcell factor between the narrow and wide series it is not surprising that no effect on the decay rate is measured for the latter series. On the other hand, this suggests that decreasing the width will result in larger enhancements of the radiative decay rate.

Further analysis of these results could comprise taking into account the ensemble distribution of decay rates, the spatial overlap between the cavity mode profile and the Er distribution and the variation in coupling ratio to modes other than the  $\text{TE}_{11}$  mode, for off-resonant arrays.

## 5.5 Conclusion

While we observed an increased radiative decay rate for the narrow series of annular apertures there is no noticeable increase of the decay rate for the wide series. This is to be expected based on the difference in  $Q/V$  between the series and the observed LDOS-dependent decay rate enhancement of a factor 4.1 for the narrow series.

# Bibliography

- [1] E. Fermi, *Quantum Theory of Radiation*, Rev. Mod. Phys. **4**, 87 (1932).
- [2] H. Raether, *Surface Plasmons on Smooth and Rough Surfaces and on Gratings (Springer Tracts in Modern Physics)*, volume 111, Springer-Verlag, Berlin Heidelberg, 1988.
- [3] W. L. Barnes, A. Dereux, and T. W. Ebbesen, *Surface plasmon subwavelength optics*, Nature **424**, 824 (2003).
- [4] A. Polman, *Erbium implanted thin film photonic materials*, Journal of Applied Physics **82**, 1 (1997).
- [5] J. N. Farahani, D. W. Pohl, H.-J. Eisler, and B. Hecht, *Single Quantum Dot Coupled to a Scanning Optical Antenna: A Tunable Superemitter*, Phys. Rev. Lett. **95**, 017402 (2005).
- [6] I. Gryczynski, J. Malicka, E. Holder, N. DiCesare, and J. R. Lakowicz, *Effects of metallic silver particles on the emission properties of  $[Ru(bpy)_3]^{2+}$* , Chem. Phys. Lett. **372**, 409 (2003).
- [7] H. Mertens, J. S. Biteen, H. A. Atwater, and A. Polman, *Polarization-Selective Plasmon-Enhanced Silicon Quantum-Dot Luminescence*, Nano Lett. **6**, 2622 (2006).
- [8] H. Mertens and A. Polman, *Plasmon-enhanced erbium luminescence*, Appl. Phys. Lett. **89**, 211107 (2006).
- [9] S. Kühn, U. Håkanson, L. Rogobete, and V. Sandoghdar, *Enhancement of Single-Molecule Fluorescence Using a Gold Nanoparticle as an Optical Nanoantenna*, Phys. Rev. Lett. **97**, 017402 (2006).
- [10] F. Tam, G. P. Goodrich, B. R. Johnson, and N. J. Halas, *Plasmonic Enhancement of Molecular Fluorescence*, Nano Lett. **7**, 496 (2007).
- [11] O. L. Muskens, V. Giannini, J. A. Sanchez-Gil, and J. Gomez Rivas, *Strong Enhancement of the Radiative Decay Rate of Emitters by Single Plasmonic Nanoantennas*, Nano Lett. **7**, 2871 (2007).
- [12] R. M. Bakker, V. P. Drachev, Z. Liu, H.-K. Yuan, R. H. Pedersen, A. Boltasseva, J. Chen, J. Irudayaraj, A. V. Kildishev, and V. M. Shalae, *Nanoantenna array-induced fluorescence enhancement and reduced lifetimes*, New Journal of Physics **10**, 125022 (2008).
- [13] F. I. Baida and D. Van Labeke, *Light transmission by subwavelength annular aperture arrays in metallic films*, Opt. Commun. **209**, 17 (2002).
- [14] F. Baida, D. Van Labeke, G. Granet, A. Moreau, and A. Belkhir, *Origin of the super-enhanced light transmission through a 2-D metallic annular aperture array: a study of photonic bands*, Applied Physics B: Lasers and Optics **79**, 1 (2004).
- [15] W. Fan, S. Zhang, B. Minhas, K. J. Malloy, and S. R. J. Brueck, *Enhanced Infrared Transmission through Subwavelength Coaxial Metallic Arrays*, Phys. Rev. Lett. **94**, 033902 (2005).
- [16] E. M. Purcell, *Spontaneous emission probabilities at radio frequencies*, Phys. Rev. **69**, 681 (1946).
- [17] Y. Liu and S. Blair, *Fluorescence enhancement from an array of subwavelength metal apertures*, Opt. Lett. **28**, 507 (2003).
- [18] S. H. Garrett, L. H. Smith, and W. L. Barnes, *Fluorescence in the presence of metallic hole arrays*, Journal of Modern Optics **52**, 1105 (2005).
- [19] A. G. Brolo, S. C. Kwok, M. G. Moffitt, R. Gordon, J. Riordon, and K. L. Kavanagh, *Enhanced Fluorescence from Arrays of Nanoholes in a Gold Film*, J. Am. Chem. Soc. **127**, 14936 (2005).
- [20] J. Wenger, D. Gérard, J. Dintinger, O. Mahboub, N. Bonod, E. Popov, T. W. Ebbesen, and H. Rigneault, *Emission and excitation contributions to enhanced single molecule fluorescence by gold nanometric apertures*, Opt. Express **16**, 3008 (2008).
- [21] URL: [www.srim.org](http://www.srim.org).

- [22] J. Kalkman, L. Kuipers, A. Polman, and H. Gersen, *Coupling of Er ions to surface plasmons on Ag*, Appl. Phys. Lett. **86**, 041113 (2005).
- [23] M. J. A. de Dood, J. Knoester, A. Tip, and A. Polman, *Förster transfer and the local optical density of states in erbium-doped silica*, Phys. Rev. B **71**, 115102 (2005).
- [24] M. J. A. de Dood, L. H. Slooff, A. Polman, A. Moroz, and A. van Blaaderen, *Local optical density of states in SiO<sub>2</sub> spherical microcavities: Theory and experiment*, Phys. Rev. A **64**, 033807 (2001).
- [25] E. Snoeks, A. Lagendijk, and A. Polman, *Measuring and Modifying the Spontaneous Emission Rate of Erbium near an Interface*, Phys. Rev. Lett. **74**, 2459 (1995).
- [26] S. Maier, *Effective Mode Volume of Nanoscale Plasmon Cavities*, Optical and Quantum Electronics **38**, 257 (2006).
- [27] Y. C. Jun, R. D. Kekatpure, J. S. White, and M. L. Brongersma, *Nonresonant enhancement of spontaneous emission in metal-dielectric-metal plasmon waveguide structures*, Phys. Rev. B **78**, 153111 (2008).
- [28] D. Van Labeke, D. Grard, B. Guizal, F. I. Baida, and L. Li, *An angle-independent Frequency Selective Surface in the optical range*, Opt. Express **14**, 11945 (2006).
- [29] E. Verhagen, L. Kuipers, and A. Polman, *Field enhancement in metallic subwavelength aperture arrays probed by erbium upconversion luminescence*, Opt. Express **17**, 14586 (2009).
- [30] J. A. Dionne, L. A. Sweatlock, H. A. Atwater, and A. Polman, *Plasmon slot waveguides: Towards chip-scale propagation with subwavelength-scale localization*, Phys. Rev. B **73**, 035407 (2006).
- [31] P. B. Johnson and R. W. Christy, *Optical Constants of the Noble Metals*, Phys. Rev. B **6**, 4370 (1972).
- [32] *Lumerical FDTD Solutions 6.0*.
- [33] C. Genet, M. P. van Exter, and J. P. Woerdman, *Fano-type interpretation of red shifts and red tails in hole array transmission spectra*, Optics Communications **225**, 331 (2003).
- [34] E. Altewischer, X. Ma, M. P. van Exter, and J. P. Woerdman, *Resonant Bragg scatter of surface plasmons on nanohole arrays*, New Journal of Physics **8**, 57 (2006).
- [35] G. N. van den Hoven, E. Snoeks, A. Polman, J. W. M. van Uffelen, Y. S. Oei, and M. K. Smit, *Photoluminescence characterization of Er-implanted Al<sub>2</sub>O<sub>3</sub> films*, Applied Physics Letters **62**, 3065 (1993).

# Acknowledgements

There are several people without whom this thesis would not have been possible; to them I owe my gratitude. First, I would like to thank my supervisors Albert Polman and Ewold Verhagen for their ideas and inspiration. I would also like to thank all members of the Photonics Materials group: Robb Walters and Rob van Loon for their experimental help, Martin Kuttge, René de Waele for interesting discussions about coaxes, Ernst Jan Vesseur for helping me with the SEM, Marc Verschuuren, Maarten Hebbink, Toon Coenen and our guest Vivian Ferry. There are many things I have learned from you all and I also want to thank you for making it a pleasant year.

Thanks to Willem Vos for allowing me to use one of his set-ups and Simon Huisman for help with those measurements. Thanks also to Femius Koenderink, Ivana Sersic, Jeroen Jacobs and Martin Frimmer for interesting work discussions and to the other members of the Center for Nanophotonics for insightful discussions and being a critical audience.

I also want to thank Chris Rétif for useful insights regarding nanofabrication, Idsart Attema for helping me with electronics, the people from the workshop and other supporting groups.

Als laatste wil ik mijn familie en vrienden bedanken. Mijn dank gaat daarbij met name uit naar mijn ouders voor het mogelijk maken van mijn studie.